The stress singularity in surfactant-driven thin-film flows. Part 2. Inertial effects

By O. E. JENSEN

Department of Applied Mathematics and Theoretical Physics, University of Cambridge,
Silver Street, Cambridge CB3 9EW, UK

A localized, insoluble, surfactant monolayer, spreading under the action of surface-tension gradients over a thin liquid film, has at its leading edge an integrable stress singularity which renders conventional thin-film approximations locally non-uniform. Here high-Reynolds-number asymptotics are used to explore the quasi-steady two-dimensional developing flow near the monolayer tip, assuming that gravity keeps the free surface almost flat, that weak 'contaminant' surfactant regularizes the singularity and that the monolayer spreads fast enough for inertial effects to be important in a region which is long compared to the film depth but which is short compared to the length of the monolayer. It is shown how downward displacement of the inviscid core flow by the subsurface viscous boundary layer yields a non-uniform pressure distribution which, when the monolayer is spreading fast enough for cross-stream pressure gradients to be significant at its tip, creates a short free-surface hump which is the thin-film version of a Reynolds ridge. The ridge and other singular flow structures are smoothed as the monolayer slows and levels of contaminant are increased. The conditions under which lubrication theory provides a uniformly accurate approximation for this class of surfactant-spreading flows are established.

1. Introduction

An insoluble surface-active monolayer, placed on the free surface of a layer of viscous liquid, may spread spontaneously under the action of surface tension gradients. Models of spreading are typically based either upon lubrication theory (when the length L^* of the monolayer greatly exceeds the fluid depth H^*, e.g. Borgas & Grotberg 1988; Jensen & Grotberg 1992) or upon boundary-layer theory (if the monolayer spreads sufficiently rapidly and $L^* \ll H^*$, e.g. Foda & Cox 1980; Jensen 1995). If surface diffusion is negligible and the monolayer is localized, an integrable stress singularity arises at the monolayer's rigid leading edge, a structure which cannot be properly resolved within either type of long-wavelength approximation. In Part 1 of this study (Jensen & Halpern 1998), it was shown how the singularity may render lubrication theory for a slowly-spreading localized monolayer non-uniform over an $O(H^*)$ lengthscale at the monolayer tip, and the leading-order Stokes flow at the tip was computed. It was demonstrated that, if gravity is sufficiently strong to suppress film disturbances, a series of Moffatt vortices may be generated in the fluid layer ahead of the monolayer, and the nonlinear regularization of the singularity by 'contaminant' surfactant ahead of the spreading monolayer was described.

Since monolayers typically slow as they spread, the Stokes-flow limit assumed in Part 1 will only be valid sufficiently late in spreading for inertial effects to be negligible.

The purpose of the present paper is to examine the effect of the stress singularity on the structure of the flow near the monolayer tip at earlier times, when the monolayer is long compared to the film depth (so that $\epsilon = H^*/L^* \ll 1$), but the tip is advancing sufficiently rapidly for both viscous and inertial forces to be locally dominant. The analysis is based on the following three key assumptions. First, gravity is assumed to be sufficiently strong for film deformations over $O(L^*)$ lengthscales to be suppressed (the 'flat-film' approximation described in Part 1); this requires $\mathscr{G} = \rho^* g^* H^{*2}/S_0^* \gg 1$, where ρ^* is the density of the fluid layer, g^* the acceleration due to gravity and S_0^* the spreading coefficient of the monolayer (i.e. the surface-tension difference driving the spreading flow). In this limit, which is readily achieved experimentally, there is a 'return' flow beneath most of the monolayer; this flow is bidirectional in the laboratory frame. Second, since (as is typical of developing flows, e.g. Van Dyke 1971) inertial effects operate at the monolayer tip over a lengthscale $O(H^*\tilde{\mathscr{R}})$ (where the Reynolds number $\tilde{\mathscr{R}} = \rho^* H^* V^*/\mu^*$, μ^* is the fluid's viscosity and V^* is the speed of advance of the monolayer tip), we assume $1 \ll \tilde{\mathscr{R}} \ll 1/\epsilon$, so that inertia is dominant in a region long compared to the film depth but short compared to the monolayer length; we may then approximate much of the quasi-steady flow in this region using the boundary-layer equations. Third, we introduce weak 'contaminant' surfactant ahead of the spreading monolayer, which regularizes the stress singularity. The contaminant concentration is expressed in terms of an inverse capillary number $\tilde{\gamma} = S_\infty^*/(V^*\mu^*)$, where $S_\infty^*(\ll S_0^*)$ is the surface-tension difference between a clean and a contaminated interface. Since contaminant effects balance viscous forces at the monolayer tip over a lengthscale $\tilde{\gamma}H^*$ (Jensen & Grotberg 1992; Part 1), we focus here primarily on the limit $1 \ll \tilde{\gamma} \ll 1/\epsilon$, again restricting attention to quasi-steady flows having horizontal lengthscales substantially shorter than L^*.

If $\mathscr{G} \gg 1$, $1 \ll \tilde{\mathscr{R}} \ll 1/\epsilon$ and $\tilde{\gamma} = 0$, the leading edge of a localized monolayer acts like a rigid plate so that beneath its tip is a Blasius boundary layer, illustrated as region I in figure 1. Since restoring forces prevent vertical displacement of the free surface, the relatively stagnant fluid (in the frame of the monolayer tip) in the subsurface boundary layer displaces the oncoming inviscid flow in the core of the fluid layer downwards and accelerates it (region II), generating a streamwise pressure gradient which drives a weaker viscous boundary layer along the lower rigid plane (region III). These boundary layers grow in thickness as the distance from the monolayer tip increases, merge (in region IV) and quickly develop into a viscous (return) flow described by lubrication theory. Similar flow structures have been identified in studies of entry flows in plane slider bearings (e.g. Tuck & Bentwich 1983; Wilson & Duffy 1998) and in high-Reynolds-number flows in channels with splitter plates (Smith 1977; Badr *et al.* 1985). Indeed, the flow sketched in figure 1 is exactly equivalent to that in which a semi-infinite splitter plate moves steadily down the centre of a channel, but surprisingly this problem does not appear to have been treated previously for non-zero Reynolds numbers. Some key aspects of the developing-flow problem illustrated in figure 1 are described in §3 below.

Weak contaminant is then introduced ahead of the monolayer, allowing us to construct asymptotically uniform solutions that show a non-trivial interaction between inertia, contaminant and the (weakened) viscous stress singularity. With contaminant present, the monolayer no longer has a well-defined leading edge; there is instead a smooth transition between stress-free conditions (as $x \to -\infty$) and a nearly rigid monolayer (as $x \to \infty$); the lengthscale of this transition is controlled by the value of $\tilde{\gamma}$. It will be shown in §4 how, provided $\tilde{\gamma}$ is not too large, the strong downward displacement of the core flow beneath the tip of the nearly-rigid section of the
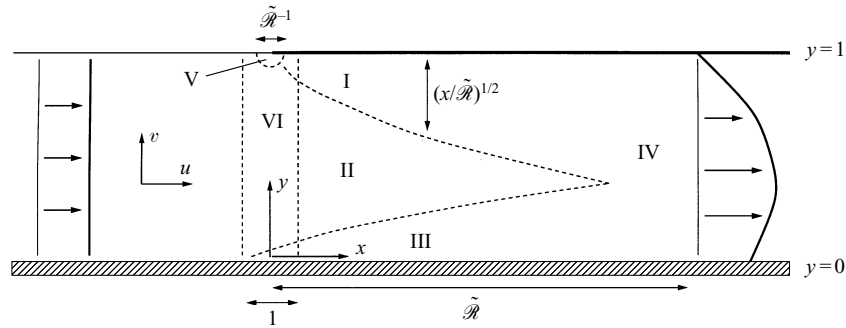
FIGURE 1. (*a*) The asymptotic quasi-steady flow structure at the tip of a localized monolayer on a flat film at high Reynolds numbers ($\tilde{\mathscr{R}} \gg 1$), in the frame in which the monolayer's rigid tip (lying along $x > 0$, $y = 1$) is stationary; the plane wall at $y = 0$ moves from left to right. Lengths are scaled on the film depth H^*. A plug flow beneath a clean, stress-free interface (upstream, $x \to -\infty$) develops into a return flow beneath a rigid interface (downstream). Region I is a nonlinear Blasius boundary layer, II is the inviscid, accelerating core flow, III is a linear boundary layer; these merge into region IV where $x = O(\tilde{\mathscr{R}})$. The surface shear stress is singular within region V; vertical pressure variations in the core appear at leading order only within region VI.

monolayer may generate an inviscid upstream response in the core, which manifests itself as a short region of elevated pressure and correspondingly a free-surface hump, of length $O(H^*)$, which is the thin-film analogue of a Thoreau–Langton–Reynolds ridge; this ridge is a well-known feature of surfactant-driven flows of deep layers (see for example Scott 1982 and references therein), but it has not previously been described in the thin-film context. We compute it here by solving a canonical boundary-layer problem (first treated approximately by Harper & Dixon 1974) in which weak contaminant controls the structure of the leading edge of the Blasius boundary layer; the hump shape is then found by solving an elliptic problem for inviscid perturbations to the oncoming core flow. As levels of contaminant are increased, the stress singularity at the monolayer tip is smoothed over a growing lengthscale, the ridge vanishes and ultimately inertial effects are dominated by viscous forces. This evolution is explored in §5 using a simple integral approximation of the appropriate boundary-layer equations. Results are summarized in §6, where conditions for the existence of the Reynolds ridge and of the peak in shear stress are identified, and the validity of the different asymptotic approximations in Parts 1 and 2 of this study is discussed.

2. The model

Suppose a dilute surfactant monolayer of length L^* advances over a viscous fluid layer of depth H^*, density ρ^* and viscosity μ^*, so that the monolayer's tip, when resolved using thin-film theory over a lengthscale $L^* \gg H^*$, is rigid and advances with steady speed V^*. An inviscid gas above the fluid layer has no influence on the motion; gravity is assumed to be sufficiently strong to suppress signficant film deformations. Far ahead of the monolayer is a contaminant surfactant having concentration $\Gamma^*_\infty \geqslant 0$. We work in the frame of the advancing monolayer, choosing a coordinate system as shown in figure 1, which illustrates the flow structure in the case $\Gamma^*_\infty = 0$. Scaling velocities on V^*, lengths on H^*, the pressure in excess of hydrostatic on $\mu^* V^*/H^*$, the surfactant concentration on $\mu^* V^*/A^*$ (where $A^* = -\mathrm{d}\sigma^*/\mathrm{d}\Gamma^* > 0$ is the surface activity, assumed constant), the quasi-steady velocity field $\boldsymbol{u}(x, y) = (u, v)$ and pressure

field $p(x, y)$ satisfy, in $-\infty < x < \infty$, $0 \leqslant y \leqslant 1$,

$$\nabla \cdot \boldsymbol{u} = 0, \quad \tilde{\mathscr{R}}\boldsymbol{u} \cdot \nabla \boldsymbol{u} = -\nabla p + \nabla^2 \boldsymbol{u}, \quad \boldsymbol{u}(x, 0) = (1, 0), \quad \int_0^1 u \, \mathrm{d}y = 1, \qquad (2.1a\text{--}d)$$

where $\tilde{\mathscr{R}} = \rho^* V^* H^* / \mu^*$. In terms of a streamfunction $\psi(x, y)$, for which $\boldsymbol{u} = (\psi_y, -\psi_x)$, the uniform-flux condition (2.1d) implies that $\psi(x, 0) = 0$, $\psi(x, 1) = 1$. The free-surface boundary conditions at $y = 1$ are

$$v = 0, \quad u_y = -\Gamma_x, \quad \Gamma u = \tilde{\gamma}. \qquad (2.2a\text{--}c)$$

These are, respectively, the kinematic condition, the tangential stress condition and the transport equation for the surfactant concentration $\Gamma(x)$. The latter has been integrated so that the surface flux of surfactant is uniform, with a value set by the strength of the dimensionless contaminant concentration $\tilde{\gamma} = \Gamma_\infty^* A^* / (\mu^* V^*)$ far upstream, ahead of the advancing monolayer. For simplicity, surface diffusion is neglected. At either end of the domain, the flow satisfies, at leading order,

$$\Gamma \sim \begin{cases} 4x \\ \tilde{\gamma}, \end{cases} \quad p \sim \begin{cases} -6x \\ 0, \end{cases} \quad \psi \sim \begin{cases} y - (y^3 - y^2) & \text{for } x \to +\infty \\ y & \text{for } x \to -\infty. \end{cases} \qquad (2.3a\text{--}c)$$

Far upstream ($x \to -\infty$) the interface is stress free, the pressure is set to zero and the oncoming velocity profile is an irrotational plug flow. Far downstream beneath the rigid monolayer is a fully developed return flow. These conditions match onto leading-order lubrication theory for a monolayer spreading on a flat film, as shown in detail in Part 1. Note that (2.1)–(2.3) and (2.5) below are identical to equations (2.15)–(2.18) in Part 1 (with $\tilde{\mathscr{D}} = 0$), except for the change of reference frame. In the singular limit $\tilde{\gamma} = 0$, we let $x = 0$ coincide with the monolayer tip, and then $\Gamma \sim 4x + \Upsilon$ as $x \to \infty$ where

$$\Upsilon = -\int_0^\infty [\psi_{yy}(x, 1) + 4] \, \mathrm{d}x. \qquad (2.4)$$

Lubrication theory then overestimates the monolayer length by an x-distance $\frac{1}{4}\Upsilon$ because it fails to resolve the stress singularity at the monolayer tip.

Since the location of the upper boundary ($y = 1$) has so far been prescribed, the normal stress condition does not enter the problem at leading order. However, it can be used to determine the shape of the perturbed free surface (at $y = h(x)$, say), by using

$$h \sim 1 + \frac{h_1}{\tilde{\mathscr{G}}}, \quad \tilde{\mathscr{G}} = \frac{\rho^* g^* H^{*2}}{\mu^* V^*}, \quad h_1 = p(x, 1) + 2u_x(x, 1) \qquad (2.5)$$

as $\tilde{\mathscr{G}} \to \infty$ (Part 1), where g^* is the gravitational acceleration. Since the speed V^* at which a long monolayer advances is $O(\epsilon S_0^* / \mu)$ (Part 1), we may write $\tilde{\mathscr{G}} = \mathscr{G} / \epsilon$, and the conditions $\epsilon \ll 1$, $\mathscr{G} \gg 1$ which ensure that the monolayer is long and flat along its entire length readily ensure that $\tilde{\mathscr{G}} \gg 1$. Under typical conditions capillary effects may be neglected (Part 1), as may a small and slowly varying quantity (denoted $\mathscr{H}$ in Part 1) which may be added to h_1 to ensure matching with an unsteady gravity-driven flow ahead of the monolayer.

Balancing inertial and viscous terms in (2.1b) assuming $u = O(1)$, and combining (2.2b,c) with $y = O(1)$, we see the emergence of x-lengthscales of magnitude $\tilde{\mathscr{R}}$ and $\tilde{\gamma}$ respectively, both of which may be long under the conditions of the model ($1 \ll \tilde{\mathscr{R}} \ll 1/\epsilon$, $0 \leqslant \tilde{\gamma} \ll 1/\epsilon$). The boundary-layer equations apply over the long

$O(\tilde{\mathscr{R}})$ lengthscale. Setting $x = \tilde{\mathscr{R}}\bar{x}$ and $(u, v, \psi, p, \Gamma) = (\bar{u}, \bar{v}/\tilde{\mathscr{R}}, \bar{\psi}, \tilde{\mathscr{R}}\bar{p}, \tilde{\mathscr{R}}\bar{\Gamma})$, (2.1), (2.2) with error $O(\tilde{\mathscr{R}}^{-2})$ become

$$\bar{\psi}_y \bar{\psi}_{y\bar{x}} - \bar{\psi}_{\bar{x}} \bar{\psi}_{yy} = -\bar{p}_{\bar{x}} + \bar{\psi}_{yyy}, \quad \bar{\psi}(\bar{x}, 0) = 0, \quad \bar{\psi}_y(\bar{x}, 0) = 1, \quad \bar{\psi}(\bar{x}, 1) = 1, \quad (2.6)$$

with a new parameter, an inverse contaminant Weber number,

$$\mathscr{J} = \frac{\tilde{\gamma}}{\tilde{\mathscr{R}}} = \frac{S_\infty^*}{\rho^* H^* V^{*2}} \tag{2.7}$$

appearing in the boundary conditions,

$$\bar{p} = \bar{p}(\bar{x}), \quad \bar{\Gamma}(\bar{x})\bar{\psi}_y(\bar{x}, 1) = \mathscr{J}, \quad \bar{\psi}_{yy}(\bar{x}, 1) = -\bar{\Gamma}_{\bar{x}}. \tag{2.8a–c}$$

Thus under suitable conditions, the Navier–Stokes problem (2.1)–(2.3) with two parameters $\tilde{\mathscr{R}}$ and $\tilde{\gamma}$ reduces to a problem for the boundary-layer equations (2.6)–(2.8) with a single parameter $\mathscr{J}$. We explore the limits $\mathscr{J} = 0$ in §3, $0 < \mathscr{J} \ll 1$ in §4 and $\mathscr{J} = O(1)$ in §5 below.

3. The developing flow beneath a localized monolayer

The general flow structure in the absence of contaminant ($\tilde{\gamma} = \mathscr{J} = 0$) is shown in figure 1, taking $x = 0$ to be the monolayer tip. A scaling analysis for this problem may be summarized as follows. For $\tilde{\mathscr{R}}^{-1} \ll x \ll \tilde{\mathscr{R}}$, a Blasius boundary layer (region I in figure 1) of thickness $O(\delta)$ exists beneath the monolayer, where $\delta = (x/\tilde{\mathscr{R}})^{1/2}$. This relatively stagnant region beneath the non-deforming free surface displaces the oncoming core fluid downwards with speed $O((x\tilde{\mathscr{R}})^{-1/2})$, and a three-layer vertical structure develops, with an inviscid, irrotational core flow (region II) and a weak passive boundary layer on the lower wall, also of thickness $O(\delta)$ (region III). Region III arises because the core flow must accelerate as it squeezes beneath region I, so downstream of the monolayer tip the pressure falls in the streamwise direction like $-\tilde{\mathscr{R}}\delta = -(x\tilde{\mathscr{R}})^{1/2}$ (this arises from the balance $\tilde{\mathscr{R}}uu_x \sim -p_x$ in (2.1b) with $u \sim 1 + O(\delta)$). The full Navier–Stokes equations apply in a region of width $O(\tilde{\mathscr{R}}^{-1})$ around the monolayer tip (region V), embedded in which is a viscous stress singularity of the form discussed in Part 1 (see also Carrier & Lin 1948; van de Vooren & Dijkstra 1970; Tayler 1973); an $O(1)$ downward flow is generated in this short region. Within an $O(1)$ distance of the monolayer tip (region VI), vertical pressure variations of $O(\tilde{\mathscr{R}}^{1/2})$ due to streamline curvature are important in the core, so that the core flow can exhibit an upstream inviscid response to the oncoming monolayer. The large pressure fluctuations close to the monolayer tip, and those of $O(\tilde{\mathscr{R}})$ further downstream (where $x = O(\tilde{\mathscr{R}})$), generate deflections of the surface of at most $O(\tilde{\mathscr{R}}/\tilde{\mathscr{G}})$ (see (2.5)) which remain small provided $\mathscr{G} \gg 1$, since $\mathscr{G} = \epsilon\tilde{\mathscr{G}}$ and $\tilde{\mathscr{R}} \ll 1/\epsilon$. For $1 \ll x \ll \tilde{\mathscr{R}}$, the pressure is uniform at leading order across the fluid layer and the boundary layers remain distinct. For $x = O(\tilde{\mathscr{R}})$, regions I–III merge into region IV, and the boundary-layer equations (2.6)–(2.8) apply across the entire flow, as is typical of developing flow problems (e.g. Schlichting 1968). The return-flow profile with a uniform pressure gradient emerges for $x \gg \tilde{\mathscr{R}}$.

3.1. *The flow in regions I–IV for* $\tilde{\gamma} = 0$, $1 \ll \tilde{\mathscr{R}} \ll 1/\epsilon$

We can therefore use (2.6)–(2.8) with $\mathscr{J} = 0$, and the classical methods of Schlichting (1968, where a more detailed account of the techniques used here may be found), Smith (1977) and Badr *et al.* (1985), to describe much of the developing flow shown in figure 1. For a similar approach to a related slider-bearing problem see Wilson &

Duffy (1998). The three-layer structure of regions I–III emerges as $\bar{x} \to 0$. The upper boundary layer in $\tilde{\mathcal{R}}^{-1} \ll \bar{x} \ll 1$ is obtained by writing $\bar{\psi}(\bar{x}, y) = 1 - \bar{x}^{1/2} F(\bar{x}, \eta)$, $\eta = (1 - y)/\bar{x}^{1/2}$, so that (2.6) becomes

$$\bar{x}\left(F_\eta F_{\eta\bar{x}} - F_{\eta\eta} F_{\bar{x}}\right) - \tfrac{1}{2} F F_{\eta\eta} = -\bar{x}\bar{p}_{\bar{x}} + F_{\eta\eta\eta}, \tag{3.1}$$

with $F(\bar{x}, 0) = 0$, $F_\eta(\bar{x}, 0) = 0$. The lower boundary layer has $\bar{\psi}(\bar{x}, y) = \bar{x}^{1/2} \hat{F}(\bar{x}, \hat{\eta})$, $\hat{\eta} = y/\bar{x}^{1/2}$, which yields (3.1) with F replaced by $\hat{F}$, subject to $\hat{F}(\bar{x}, 0) = 0$, $\hat{F}_{\hat{\eta}}(\bar{x}, 0) = 1$. In each boundary layer we must apply suitable conditions to match with the core flow.

We expand in powers of $\bar{x}^{1/2}$, so that in the core (region II)

$$\bar{\psi} = \bar{\psi}_0(y) + \bar{x}^{1/2} \bar{\psi}_1(y) + O(\bar{x}), \quad \bar{p} = \bar{x}^{1/2} \bar{p}_0 + O(\bar{x}) \tag{3.2a,b}$$

and $\bar{\Gamma} = \bar{x}^{1/2}\bar{\Gamma}_0 + \bar{x}\bar{\Gamma}_1 + O(\bar{x}^{3/2})$. It follows from (2.6)–(2.8) that $\bar{\psi}_0 = y$ (the oncoming plug flow) and $\bar{\psi}_1 = -\bar{p}_0 y$ (an inviscid correction driven by the Blasius boundary layer). In the upper boundary layer (region I), we set $F = F_0(\eta) + \bar{x}^{1/2} F_1(\eta) + O(\bar{x})$, so that (3.1) gives

$$-\tfrac{1}{2} F_0 F_0'' = F_0''' \quad \text{and} \quad \tfrac{1}{2}(F_0' F_1' - F_0 F_1'') - F_1 F_0'' = -\tfrac{1}{2}\bar{p}_0 + F_1''', \tag{3.3a,b}$$

with $F_i(0) = 0$, $F_i'(0) = 0$ for $i = 0, 1$. The leading-order contribution F_0 is the usual Blasius function. In the far field, $F_0 \sim \eta - 2C$ as $\eta \to \infty$, so that at the outer edge of the Blasius boundary layer is an induced downward flow with vertical velocity $-C/\bar{x}^{1/2}$, where $C \approx 0.8604$. Matching with the induced core flow $\bar{\psi}_1$ implies that $\bar{p}_0 = -2C$. The streamfunction at next order, F_1, driven by the induced pressure gradient in (3.3b), is also readily computed (this was done using a simple finite-difference method), applying $F_{1\eta} \sim -\bar{p}_0$ as $\eta \to \infty$. The surfactant distribution then satisfies $\bar{\Gamma}_0 = 2F_0''(0) \approx 0.66412$, $\bar{\Gamma}_1 = F_1''(0) \approx 1.8967$. In the lower boundary layer (region III), we expand using $\hat{F} = \hat{\eta} + \bar{x}^{1/2} \hat{F}_1(\hat{\eta}) + \ldots$, so that (3.1) yields $\tfrac{1}{2}\hat{F}_1' - \tfrac{1}{2}\hat{\eta}\hat{F}_1'' = -\tfrac{1}{2}\bar{p}_0 + \hat{F}_1'''$, with $\hat{F}_1(0) = 0$, $\hat{F}_1'(0) = 0$ and $\hat{F}_1'(\hat{\eta}) \to -\bar{p}_0$ as $\hat{\eta} \to \infty$. This is a linear self-similar boundary layer, driven by the external pressure gradient; $\hat{F}_1$ is also readily determined (again a finite-difference method was used). A composite expression for the streamfunction can then be constructed,

$$\bar{\psi}(\bar{x}, y) = 1 + \bar{x}^{1/2}\left[\bar{p}_0 y - F_0(\eta)\right] + \bar{x}\left[\hat{F}_1(\hat{\eta}) - F_1(\eta)\right] + \ldots \quad \text{as} \quad \bar{x} \to 0, \tag{3.4}$$

from which the leading-order velocity profile can be computed. Some developing profiles for $10^{-4} \leqslant \bar{x} \leqslant 0.005$ are shown in figure 2, illustrating how the boundary layers thicken very rapidly as $\bar{x}$ increases. These profiles for small $\bar{x}$ are more illustrative than realistic, since the condition $x = \tilde{\mathcal{R}}\bar{x} \gg 1$ implicit in this approximation puts stringent and possibly impractical bounds on acceptable Reynolds numbers.

Further downstream in region IV, we can perturb about the fully-developed return flow, $\psi_\infty(y) = y - (y^3 - y^2)$, by setting $\bar{\psi} = \psi_\infty(y) + e^{-\hat{\alpha}\bar{x}}\phi(y)$, where $\text{Re}(\hat{\alpha}) > 0$ and $\bar{x}$ is sufficiently large to ensure that $e^{-\hat{\alpha}\bar{x}} \ll 1$. Then (2.6) becomes an Orr–Sommerfeld problem

$$\phi_{yyyy} + \hat{\alpha}\psi_{\infty y}\phi_{yy} - \hat{\alpha}\psi_{\infty yyy}\phi = 0, \quad \phi(0) = \phi(1) = \phi_y(0) = \phi_y(1) = 0. \tag{3.5}$$

The most slowly decaying eigenvalue for the return-flow case has been given by Stocker & Duck (1995) as $\hat{\alpha} = 46.077$ in a channel of double the width. In finite-difference computations we found $\hat{\alpha} = 48.3349$. Three examples of the perturbed return flow are shown with broken lines in figure 2; in the figure, $\phi_{yy}(\bar{x}, 0) = 1$ was
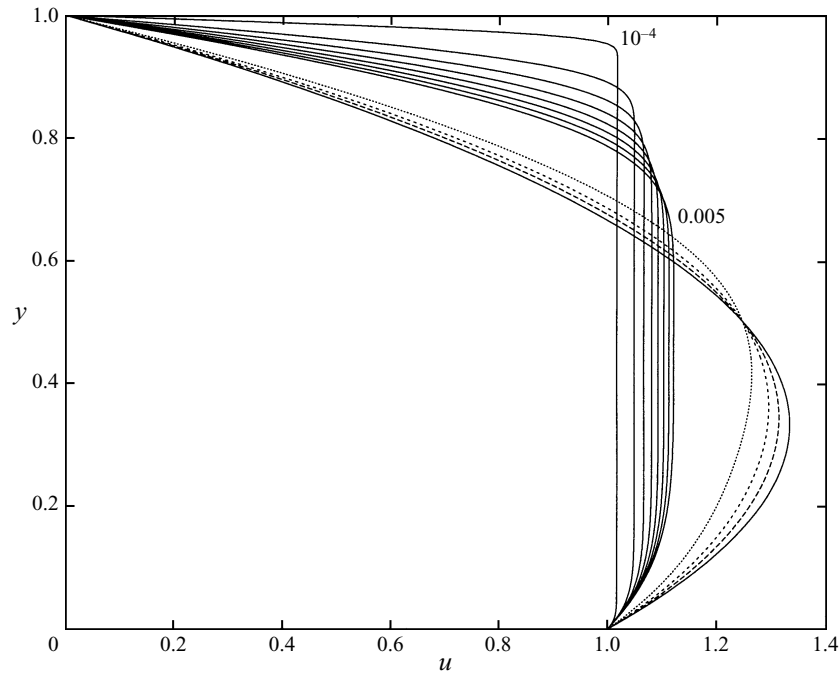
FIGURE 2. The return-flow profile (solid, $u = 1-3y^2+2y$) is shown together with eight boundary-layer profiles (solid lines, see (3.4)), corresponding to equal $\bar{x}$-spacings between $\bar{x} = 10^{-4}$ and 0.005, and with three downstream perturbations (broken lines, see (3.5)); the latter are separated by $\bar{x}$-distances $(\log 2)/\hat{\alpha} \approx 0.0143$.

chosen to normalize the eigenfunction, and $\psi_{\infty y} - k\phi_y$ was plotted for $k = 0.1$, 0.2 and 0.4, corresponding to changes in $\bar{x}$ between each curve of 0.0143. The large value of $\hat{\alpha}$ confirms that the flow development is very rapid on the $\bar{x}$-lengthscale.

The strong variation in the core pressure in regions II and IV perturbs the free surface. From the normal stress condition (2.2b), $h_1 \sim \bar{p}_0(\tilde{\mathcal{R}}x)^{1/2}$ for $1 \ll x \ll \tilde{\mathcal{R}}$, where $\bar{p}_0 \approx -1.721$; here the pressure distribution is controlled by inertial effects as the core flow accelerates. Further away from the monolayer tip, once $x \gg \tilde{\mathcal{R}}$, a linearly diminishing pressure distribution is required to balance viscous forces, so that $h_1 \sim -6x + \hat{C}$, for some constant $\hat{C}$, to match onto its distribution given by lubrication theory (see Part 1, equation 2.8). Computation of $\hat{C}$ is beyond the scope of the present study. The intermediate flow structure, for $x = O(\tilde{\mathcal{R}})$, connecting the two approximations in figure 2 may be obtained by solving (2.6)–(2.8) numerically. However, since the development length is so short on the $\bar{x}$-lengthscale, very high Reynolds numbers are likely to be required for there to be sufficiently great separation of lengthscales to ensure accuracy of the asymptotic model. This implies for example that the approximation $\mathit{\Upsilon} \approx \overline{\mathit{\Upsilon}}\tilde{\mathcal{R}}$ for the monolayer length correction (see (2.4)), where $\overline{\mathit{\Upsilon}} = -\int_0^\infty [\bar{\psi}_{yy}(\bar{x}, 1) + 4]\, d\bar{x}$, is likely to be poor for modest values of $\tilde{\mathcal{R}}$. (The value of $\overline{\mathit{\Upsilon}}$ may be estimated by patching, at $\bar{x} = \bar{x}_0$, say, the two asymptotic expressions $\overline{\mathit{\Gamma}} \sim \bar{x}^{1/2}\overline{\mathit{\Gamma}}_0 + \bar{x}\overline{\mathit{\Gamma}}_1$ and $\overline{\mathit{\Gamma}} \sim 4\bar{x} + \overline{\mathit{\Upsilon}} + \overline{A}\,\mathrm{e}^{-\hat{\alpha}\bar{x}}$ for some $\overline{A}$; ensuring continuity of $\overline{\mathit{\Gamma}}$ and $\overline{\mathit{\Gamma}}_{\bar{x}}$ we found that $0.06 < \mathit{\Upsilon} < 0.09$ for $0.05 < \bar{x}_0 < 0.02$.) The constraints of the present problem ($1 \ll \tilde{\mathcal{R}} \ll 1/\epsilon$) put an upper bound on $\tilde{\mathcal{R}}$, such that in most practical circumstances a solution of the singular Navier–Stokes problem (2.1)–(2.3) with $\tilde{\gamma} = 0$ is likely to be more appropriate, and would also reveal the pressure
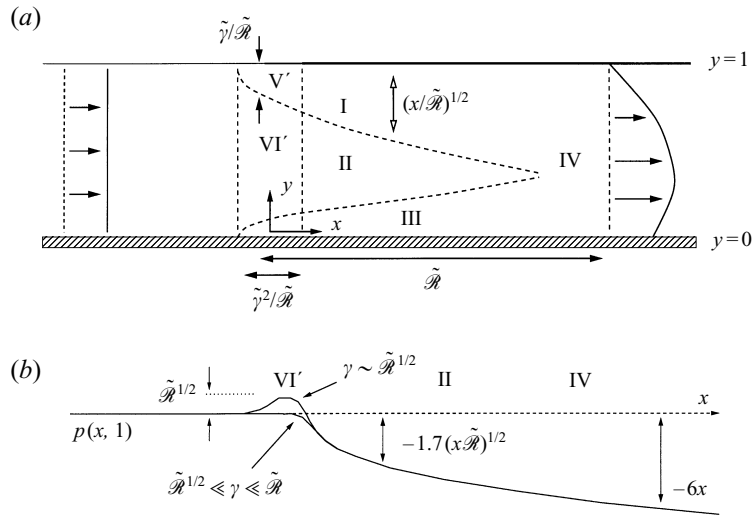
FIGURE 3. (*a*) The asymptotic flow structure with contaminant, when $1 \ll \tilde{\gamma} \ll \tilde{\mathscr{R}}$. (*b*) A sketch of the corresponding free-surface pressure distribution, which is monotonic for $\tilde{\gamma} \gg \tilde{\mathscr{R}}^{1/2}$, but which has a local hump, generating a Reynolds ridge, when $\tilde{\gamma} = O(\tilde{\mathscr{R}}^{1/2})$. The leading-order approximations for $p(x, 1)$ in region II and as $x \to \infty$ are also shown.

distribution close to the monolayer tip. We leave such problems for a future study, since substantial progress can instead be made by introducing weak contaminant ahead of the monolayer.

4. Contaminant effects in the limit $1 \ll \tilde{\gamma} \ll \tilde{\mathscr{R}} \ll 1/\epsilon$

Suppose now that instead of advancing over a clean interface (as in figure 1), contaminant surfactant, represented by the parameter $\tilde{\gamma}$ in (2.2)–(2.3), is present ahead of the advancing monolayer, smoothing the stress singularity. Again, we start by summarizing the results of a scaling analysis. For $1 \ll \tilde{\gamma} \ll \tilde{\mathscr{R}}$ there is a strong interaction between the leading edge of the Blasius boundary layer and the contaminant; the flow structure in this case is shown in figure 3(*a*), and sketches of the two qualitatively distinct free-surface pressure distributions that may arise are shown in figure 3(*b*). Regions V and VI in figure 1 are now replaced by regions V′ and VI′ respectively; regions I–IV (and the analysis of §3.1) are unaffected at leading order by the presence of contaminant. Seeking a dominant balance between $\tilde{\mathscr{R}}uu_x$ and u_{yy} in (2.1*b*) and between the terms in (2.2), with $u = O(1)$ and $\Gamma = O(\tilde{\gamma})$, we obtain the dimensions of region V′, which has length $\tilde{\gamma}^2/\tilde{\mathscr{R}}$ and a much shorter depth $\tilde{\gamma}/\tilde{\mathscr{R}}$; the local maximum of shear stress in this region is of magnitude $\tilde{\mathscr{R}}/\tilde{\gamma}$. Again there is downward displacement of fluid into region VI′ (with weak vertical velocity of $O(1/\tilde{\gamma})$), generating pressure fluctuations of $O(\tilde{\gamma})$ in the core, and a weak viscous boundary layer develops on the lower wall. There is no leading-order cross-stream pressure gradient anywhere in the core provided region VI′ is long, i.e. $\tilde{\mathscr{R}}^{1/2} \ll \tilde{\gamma} \ll \tilde{\mathscr{R}}$, in which case the entire developing flow may be described by the boundary-layer equations (2.6)–(2.8) with $\mathscr{J} \ll 1$; this singular limit is investigated in §4.1 below. In this case it turns out that the pressure falls monotonically with x, as sketched in figure 3(*b*); the pressure distribution in region VI′ (and region II) is controlled by inertial forces, being related directly to the displacement thickness of the boundary

layer in region V' (and region I respectively); it evolves towards the linear distribution predicted by lubrication theory as $x \to \infty$, where viscous forces are dominant. If $\tilde{\gamma} = O(\tilde{\mathcal{R}}^{1/2})$, however, there is a short-lengthscale upstream response of the inviscid core flow to the oncoming monolayer associated with horizontal *and* vertical pressure fluctuations of $O(\tilde{\mathcal{R}}^{1/2})$ in region VI'. It will be demonstrated in §4.2 below that as a result the free-surface pressure distribution has a local hump across region VI' (also sketched in figure 3b), which generates the thin-film version of a Reynolds ridge.

If $\tilde{\gamma} = O(\tilde{\mathcal{R}})$, regions I–VI' in figure 3 are no longer distinct, and the entire flow varies smoothly over a long $\tilde{\mathcal{R}}$ lengthscale. The corresponding solutions of (2.6)–(2.8) with $\mathcal{J} = O(1)$ are given in §5 below. If $\tilde{\mathcal{R}} \ll \tilde{\gamma} \ll 1/\epsilon$, then contaminant eliminates inertial effects altogether and the flow is purely viscous, being governed by the lubrication-theory solution given in figure 2 of Part 1. At the opposite extreme, if $\tilde{\gamma} = O(1)$ or smaller, a Navier–Stokes solution is required where $x = O(1)$, which is beyond the scope of the present study. We proceed, then, by considering the case in which the smoothing effect of contaminant is just powerful enough for the boundary-layer equations to apply throughout the entire flow.

4.1. *The limit* $1 \ll \tilde{\mathcal{R}}^{1/2} \ll \tilde{\gamma} \ll \tilde{\mathcal{R}} \ll 1/\epsilon$: *region* V'

If $\mathcal{J} \equiv \tilde{\gamma}/\tilde{\mathcal{R}} \ll 1$, (2.6)–(2.8) reduce to the developing-flow problem considered in §3.1 for $\bar{x} = O(1)$, but a new three-layer structure emerges as $\bar{x} \to 0$ with $x = O(\tilde{\gamma}^2/\tilde{\mathcal{R}})$. We therefore rescale (2.6)–(2.8), setting $\bar{x} = \mathcal{J}^2 \check{x}$, $\bar{\Gamma} = \mathcal{J}\check{\Gamma}$, $\bar{p} = \mathcal{J}\check{p}$. The upper boundary layer (region V' in figure 3a) is of the form $\bar{\psi} = 1 - \mathcal{J}\check{\psi}(\check{x}, \check{\eta})$ where $\check{\eta} = (1-y)/\mathcal{J}$. Expanding, with $(\check{\psi}, \check{p}, \check{\Gamma}) = (\check{\psi}_0, \check{p}_0, \check{\Gamma}_0) + O(\mathcal{J})$, the leading-order problem in this region becomes

$$\check{\psi}_{0\check{\eta}}\check{\psi}_{0\check{\eta}\check{x}} - \check{\psi}_{0\check{x}}\check{\psi}_{0\check{\eta}\check{\eta}} = \check{\psi}_{0\check{\eta}\check{\eta}\check{\eta}}, \quad \check{\psi}_{0\check{\eta}\check{\eta}}(\check{x},0) = \check{\Gamma}_{0\check{x}}(\check{x}), \quad \check{\psi}_{0\check{\eta}}(\check{x},0)\check{\Gamma}_0(\check{x}) = 1 \tag{4.1}$$

with $\check{\psi}_0(\check{x},0) = 0$ and $\check{\psi} \to \check{\eta} - \check{D}(\check{x})$ as $\check{\eta} \to \infty$, where $\check{D}$ is a function representing the upper boundary-layer's displacement thickness. Far upstream in region V', $\check{\psi}_0 \to \check{\eta}$ and $\check{\Gamma}_0 \to 1$; far downstream, with $\check{x} \gg 1$, the upper boundary layer in region V' approaches a self-similar Blasius form (with $\check{\Gamma}_0 \gg 1 \gg \check{\psi}_{0\check{\eta}}(\check{x},1)$), to match onto region I of the developing flow (3.4).

The boundary-layer problem (4.1) arises also at the leading edge of a monolayer spreading on deep fluid, and approximate solutions have been presented in this context by Harper & Dixon (1974). We solved this canonical boundary-layer problem numerically, exploiting the von Mises transformation (described, for example, in Schlichting 1968). If $\check{\psi}_{0\check{\eta}}(\check{x}, \check{\eta}) = U(\check{x}, \check{\psi}_0)$, (4.1) becomes a nonlinear diffusion equation

$$U_{\check{x}} = \left(U U_{\check{\psi}_0}\right)_{\check{\psi}_0}, \quad U U_{\check{\psi}_0}(\check{x},0) = \check{\Gamma}_{0\check{x}}(\check{x}), \quad U(\check{x},0)\check{\Gamma}_0(\check{x}) = 1 \tag{4.2}$$

with $U \to 1$ as $\check{\psi}_0 \to \infty$. Integration of (4.2) is straightforward using finite differences in $\check{\psi}_0$ and an implicit timestepping procedure; one can march in the direction of increasing $\check{x}$, using

$$U \sim 1 - \mathrm{e}^{\check{x}-\check{\psi}_0} + \left(\frac{3\mathrm{e}^{-\sqrt{2}\check{\psi}_0}}{(2-\sqrt{2})} + \tfrac{1}{2}e^{-2\check{\psi}_0}\right)\mathrm{e}^{2\check{x}}, \quad \check{\Gamma}_0 \sim 1 + \mathrm{e}^{\check{x}} - \left(\frac{3}{2(\sqrt{2}-1)} + 1\right)\mathrm{e}^{2\check{x}}$$

with $\check{x} \to -\infty$ as an upstream initial condition. By setting the coefficient of the $O(\mathrm{e}^{\check{x}})$ term to unity we fix the origin of the solution. It was verified that numerical results were independent of the location of the upstream starting point.
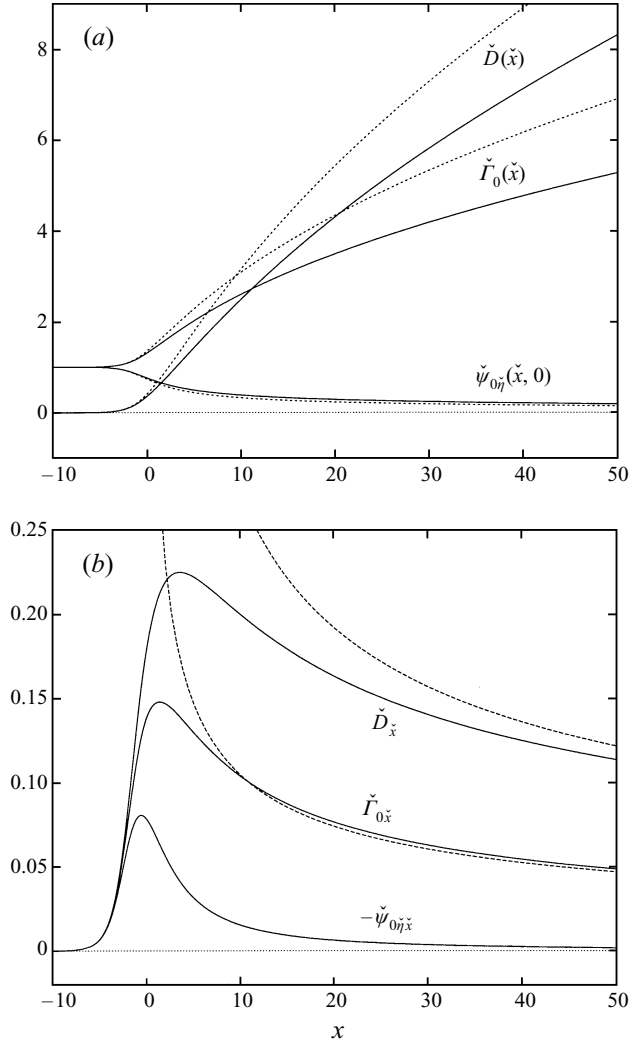
FIGURE 4. Solid lines show numerical solutions of (4.1), showing (a) surface velocity $\check{\psi}_{0\check{\eta}}(\check{x}, 0)$, surfactant concentration $\check{\Gamma}_0(\check{x})$ and displacement thickness $\check{D}(\check{x})$; (b) $-\check{\psi}_{0\check{\eta}\check{x}}(\check{x}, 0)$ (surface compression), $\check{\Gamma}_{0\check{x}}(\check{x})$ (surface shear stress) and $\check{D}_{\check{x}}(\check{x})$ (induced downward flow). Also shown in (a) (dotted) is the integral approximation (4.3a–d), and in (b) (dashed) the downstream asymptotes of $\check{\Gamma}_{\check{x}}$ [$F_0''(0)\check{x}^{-1/2}$] and $\check{D}_{\check{x}}$ [$C\check{x}^{-1/2}$].

The solution of (4.1), (4.2) is shown with solid lines in figure 4. Figure 4(a) shows how the surface velocity decreases as the surfactant concentration and displacement thickness $\check{D}(\check{x})$ increase. There are sharp peaks (figure 4b) in the surface shear stress (at $\check{x} \approx -0.48$), in the surface compression (at $\check{x} \approx 1.5$) and in the induced flow normal to the free surface $\check{D}_{\check{x}}(\check{x})$ (at $\check{x} \approx 3.7$). The latter drives an inviscid flow in the core (region VI′ in figure 3a): setting $\bar{\psi} = y + \mathscr{J}\bar{\psi}_1(\check{x}, y) + O(\mathscr{J}^2)$, (2.6)–(2.8) imply that $\bar{\psi}_1 = -y\check{p}(\check{x})$; matching implies that $\check{p}(\check{x}) = -\check{D}(\check{x})$, so the core pressure falls monotonically along region VI′ (as sketched in figure 3b), provided this region is long. The non-uniform pressure distribution in the core again gives rise to a deflection of the free surface, with $\tilde{h}_1 = -\tilde{\gamma}\check{D}(\check{x})$ locally (from (2.5)), which remains a small

perturbation provided $\mathscr{G} \ll 1$. Given the region VI$'$ pressure distribution $\check{p}(\check{x})$, one can in principle determine the flow in the lower boundary layer along $y = 0$, but this is not necessary here. Figure 4(a) also shows how the numerical solution compares with the integral approximation of Harper & Dixon (1974) which, by assuming an exponential velocity profile, gives

$$\check{x} = \left(\frac{1}{b^2} - 1\right) + \log\left[\frac{1}{2}\left(\frac{1}{b^2} - 1\right)\right], \quad \check{\psi}_{0\eta} \approx b, \quad \check{\Gamma}_0 \approx \frac{1}{b}, \quad \check{D} \approx \frac{2(1-b)}{b(1+b)}, \quad (4.3a\text{--}d)$$

and thereby captures the correct leading-order exponential decay as $\check{x} \to -\infty$ and the appropriate scaling $\check{D} \propto \check{x}^{1/2}$ as $\check{x} \to \infty$. Figure 4(a) shows that (4.3) provides a good qualitative approximation to the exact solution. Figure 4(b) shows how the solution of (4.1) matches onto the Blasius solution as $\check{x} \to \infty$, with a slowly decaying $O(\check{x}^{-3/2})$ correction.

4.2. *The Reynolds ridge: region* VI$'$ *with* $1 \ll \tilde{\gamma} \sim \tilde{\mathscr{R}}^{1/2} \ll 1/\epsilon$

We now relax the assumption that $\tilde{\gamma} \gg \tilde{\mathscr{R}}^{1/2}$, to allow for cross-stream pressure gradients in region VI$'$, but retain the condition $\tilde{\gamma} \gg 1$, ensuring that the downward vertical flow generated by region V$'$ is weak. It is convenient to introduce the parameter $\mathscr{M} \equiv \tilde{\mathscr{R}}/\tilde{\gamma}^2$. For $\mathscr{M} = O(1)$, the upper boundary layer (region V$'$) remains exactly as described in §4.1 (figure 4), generating an $O(1/\tilde{\gamma})$ downward flow, but the response of the core to its forcing by the upper boundary layer becomes non-local. We shall see that the result is an inertially-driven elevation of the free surface, which is the thin-film analogue of a Reynolds ridge.

To describe inviscid perturbations to the core flow in region VI$'$, we rescale (2.1)–(2.2), setting $u = 1 + \check{U}/\tilde{\gamma}$, $p = \check{P}/\mathscr{J}$ and $v = \check{V}/\tilde{\gamma}$. Then the leading-order equations in the core on an $O(1)$ lengthscale become

$$\check{U}_x + \check{V}_y = 0, \quad \check{U}_x = -\check{P}_x, \quad \check{V}_x = -\check{P}_y, \quad \check{V}(x, 0) = 0, \quad \check{V}(x, 1) = \check{v}_s(\mathscr{M}x), \quad (4.4a\text{--}e)$$

where $\check{v}_s(\mathscr{M}x) = \check{v}_s(\check{x}) = -\check{D}_{\check{x}}(\check{x})$ (as shown in figure 4b). Thus $\check{V}(x, y)$ satisfies Laplace's equation subject to (4.4d,e). We seek the solution for $\check{V}$ in terms of a Green's function, so that $\check{V}(x, y) = \int_{-\infty}^{\infty} \check{G}(x-s, y)\check{v}_s(\mathscr{M}s)\,\mathrm{d}s$, where $\nabla^2\check{G} = 0$, $\check{G}(x, 0) = 0$, $\check{G} \to 0$ as $x \to \pm\infty$ and $\check{G}(x, 1) = \delta(x)$. Then, since $\check{V}_y = \check{P}_x$, we can compute the pressure directly using $\check{G}$,

$$\check{p}(x, y) = -\int_{-\infty}^{\infty} \check{G}_y(x - s, y)\check{D}(\mathscr{M}s)\,\mathrm{d}s, \quad (4.5)$$

where $\check{p} = \mathscr{M}\check{P} = p/\tilde{\gamma}$. The appropriate Green's function may be shown using Fourier transforms to be (Sneddon 1974)

$$\check{G}(x, y) = \sum_{n=1}^{\infty} (-1)^{n+1} \mathrm{e}^{-n\pi|x|} \sin n\pi y = \frac{\sin \pi y}{2(\cosh \pi x + \cos \pi y)}. \quad (4.6)$$

To determine the corresponding free-surface displacement, (4.5) was evaluated in the singular limit $y \to 1$. The integral was computed numerically in two ways: using (4.5) directly, keeping $y < 1$, and verifying that this was in close agreement with the following asymptotic result:

$$\check{p}(x, 1) = \lim_{\delta \to 0}\left[\frac{1}{2}\pi\left(\int_{-\infty}^{x-\delta} + \int_{x+\delta}^{\infty}\right)\frac{\check{D}(\mathscr{M}t)\,\mathrm{d}t}{\cosh \pi(x - t) - 1} - \frac{2\check{D}(\mathscr{M}x)}{\pi\delta}\right]. \quad (4.7)$$

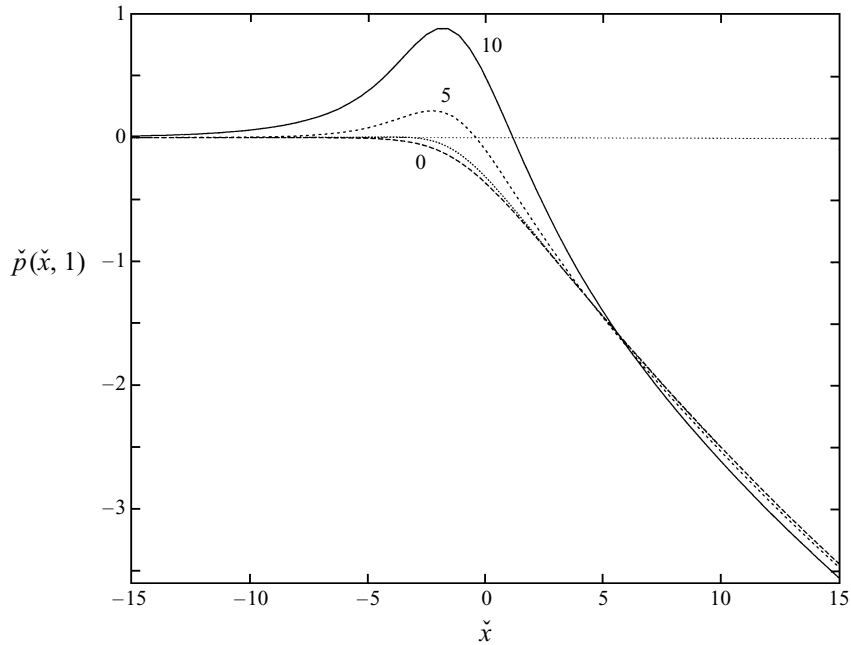Results were also verified by constructing an asymptotic approximation to (4.7)

FIGURE 5. The Reynolds ridge, showing $\check{p}(\check{x},1) = p/\tilde{\gamma}$ (see (4.7)) versus $\check{x} \equiv \mathcal{M}x$ for $\mathcal{M} \equiv \tilde{\mathcal{R}}/\tilde{\gamma}^2 = 0$ (long-dash, $\check{p} = -\check{D}(\check{x})$), $\mathcal{M} = 2$ (dotted), $\mathcal{M} = 5$ (short-dash) and $\mathcal{M} = 10$ (solid).

for small $\mathcal{M}$ (the limit in which region VI$'$ is long enough for cross-stream pressure fluctuations to be weak). With $x = \check{x}/\mathcal{M}$, $u = 1 + \mathcal{J}\check{u}_1$, $v = \check{v}/\tilde{\gamma}$ and taking $1 \ll \tilde{\gamma} \ll \tilde{\mathcal{R}}$, (4.4$a$–$e$) becomes

$$\check{u}_{1\check{x}} + \check{v}_y = 0, \quad \check{u}_{1\check{x}} = -\check{p}_{\check{x}}, \quad \mathcal{M}^2\check{v}_{\check{x}} = -\check{p}_y, \quad \check{v}(\check{x},0) = 0, \quad \check{v}(\check{x},1) = \check{v}_s(\check{x}). \qquad (4.8)$$

For $\mathcal{M} \to 0$, an expansion of (4.8) gives $\check{v}(\check{x},y) \sim \check{v}_s(\check{x})y + \frac{1}{6}\mathcal{M}^2\check{v}_{s\check{x}\check{x}}(\check{x})y(1-y^2) + O(\mathcal{M}^4)$. All terms which are $O(\mathcal{M}^4)$ or smaller may be shown to include factors $(1-y)^n$ where $n \geqslant 2$. It follows that

$$\check{p}(\check{x},1) \sim -\check{D}(\check{x}) + \tfrac{1}{3}\mathcal{M}^2\check{D}_{\check{x}\check{x}}(\check{x}) \qquad \text{as} \quad \mathcal{M} \to 0. \qquad (4.9)$$

The error in (4.9) is exponentially small for $\mathcal{M} \ll 1$, since all higher-order terms vanish along $y = 1$.

Solutions of (4.7) are shown in figure 5. For $\mathcal{M} \leqslant 1$ the ridge is almost imperceptible; as $\mathcal{M}$ increases, a Reynolds ridge develops over an $O(1)$ x-lengthscale. The approximation (4.9) turns out to be accurate for $\mathcal{M} \leqslant 1$ (that for $\mathcal{M} = 2$ is almost indistinguishable from that in figure 5, for example). Since $\check{D} \sim e^{\check{x}}$ as $\check{x} \to -\infty$, we can therefore estimate the critical value of $\mathcal{M}$ above which the free surface rises with $\check{x}$ as $\mathcal{M} \approx \sqrt{3}$. The ridge is noticeable for $\mathcal{M} = 5$, and pronounced for $\mathcal{M} = 10$. Larger values of $\mathcal{M}$ for fixed $\tilde{\mathcal{R}}$ are obtained by reducing $\tilde{\gamma}$: however, once $\tilde{\gamma}$ is $O(1)$ or smaller it is necessary to know the detailed distribution of the $O(1)$ downward velocity at the leading edge of the Blasius boundary layer, which is beyond the scope of this investigation.
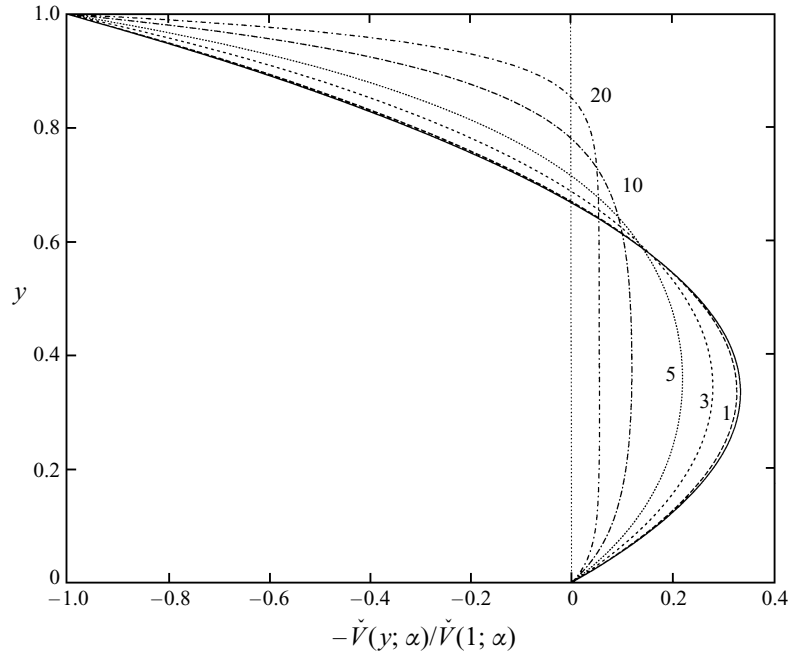
FIGURE 6. The velocity profiles of the integral model of §5.2. The normalized velocity profile $-\check{V}(y;\alpha)/\check{V}(1;\alpha)$ (see (5.3*a,b*)) is plotted for $\alpha = 1$ (dashed), 3, 5, 10, 20 (dot-dashed). The solid line shows the return-flow profile $u = -3y^2 + 2y$.

5. Contaminant effects in the limit $1 \ll \tilde{\gamma} \sim \tilde{\mathscr{R}} \ll 1/\epsilon$

Having described the limit $\mathscr{J} = \tilde{\gamma}/\tilde{\mathscr{R}} \to 0$, we now consider the full boundary-layer problem (2.6)–(2.8) with $\mathscr{J} = O(1)$. In this limit the regions shown in figure 3(*a*) are no longer distinct, although much of this six-region asymptotic structure should be recovered from what follows as $\mathscr{J}$ falls in magnitude. Here we use a simple integral approximation (§5.2), which allows a range of values of $\mathscr{J}$ to be considered relatively easily, and which allows us to bridge the gap between the singular limit considered in §4 (with $1 \ll \tilde{\gamma} \ll \tilde{\mathscr{R}}$) and lubrication theory (for which $1 \ll \tilde{\mathscr{R}} \ll \tilde{\gamma}$). We aim to show how the stress singularity first manifests itself as $\mathscr{J}$ is reduced from large values, by generating (for example) local peaks in shear stress; this approach therefore parallels §4 of Part 1. The model is motivated by the asymptotic structure of the flow far upstream, which is considered first.

5.1. *The linearized flow far upstream*

For $\bar{x} \to -\infty$, we can consider small perturbations to the oncoming plug flow. In (2.6)–(2.8) we set $\bar{\psi} \sim y + \epsilon\psi'(y)e^{\alpha^2\bar{x}}$, $\bar{p} \sim \epsilon p'e^{\alpha^2\bar{x}}$, $\bar{\Gamma} = \mathscr{J} + \epsilon\Gamma'e^{\alpha^2\bar{x}}$ for some $\epsilon \ll 1$ and some $\alpha > 0$. If we seek solutions at $O(\epsilon)$, we must solve, for $u'(y) \equiv \psi'_y$,

$$\alpha^2 u' = -\alpha^2 p' + u'_{yy}, \quad \int_0^1 u' \, dy = 1, \quad u'(0) = 0, \quad u'_y(1) = \alpha^2\mathscr{J}u'(1). \quad (5.1a\text{–}d)$$

The following eigenvalue relation for the decay rate α^2 is obtained from (5.1):

$$\mathscr{J} = \check{W}(\alpha), \qquad \check{W}(\alpha) \equiv \frac{\alpha\cosh\alpha - \sinh\alpha}{\alpha\,[2 - 2\cosh\alpha + \alpha\sinh\alpha]}, \quad (5.2)$$
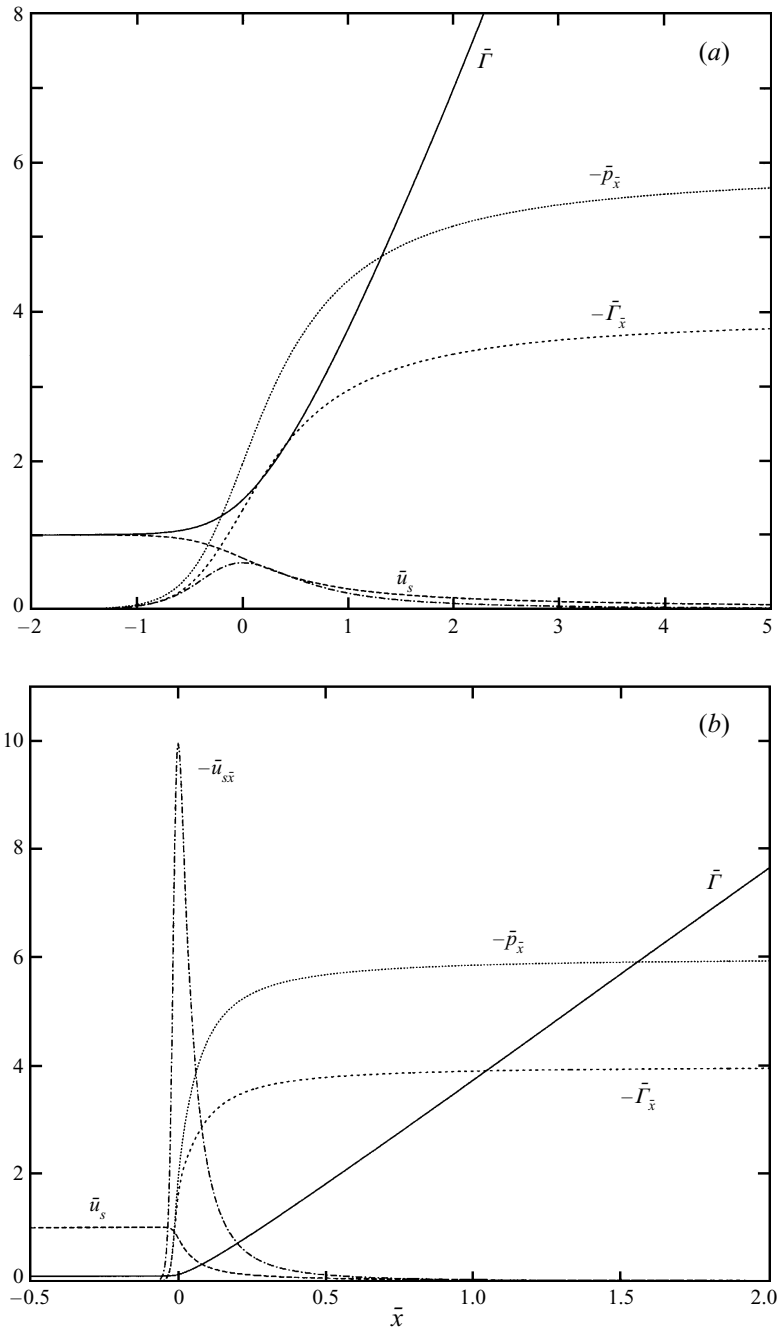
FIGURE 7 (*a,b*). For caption see facing page.

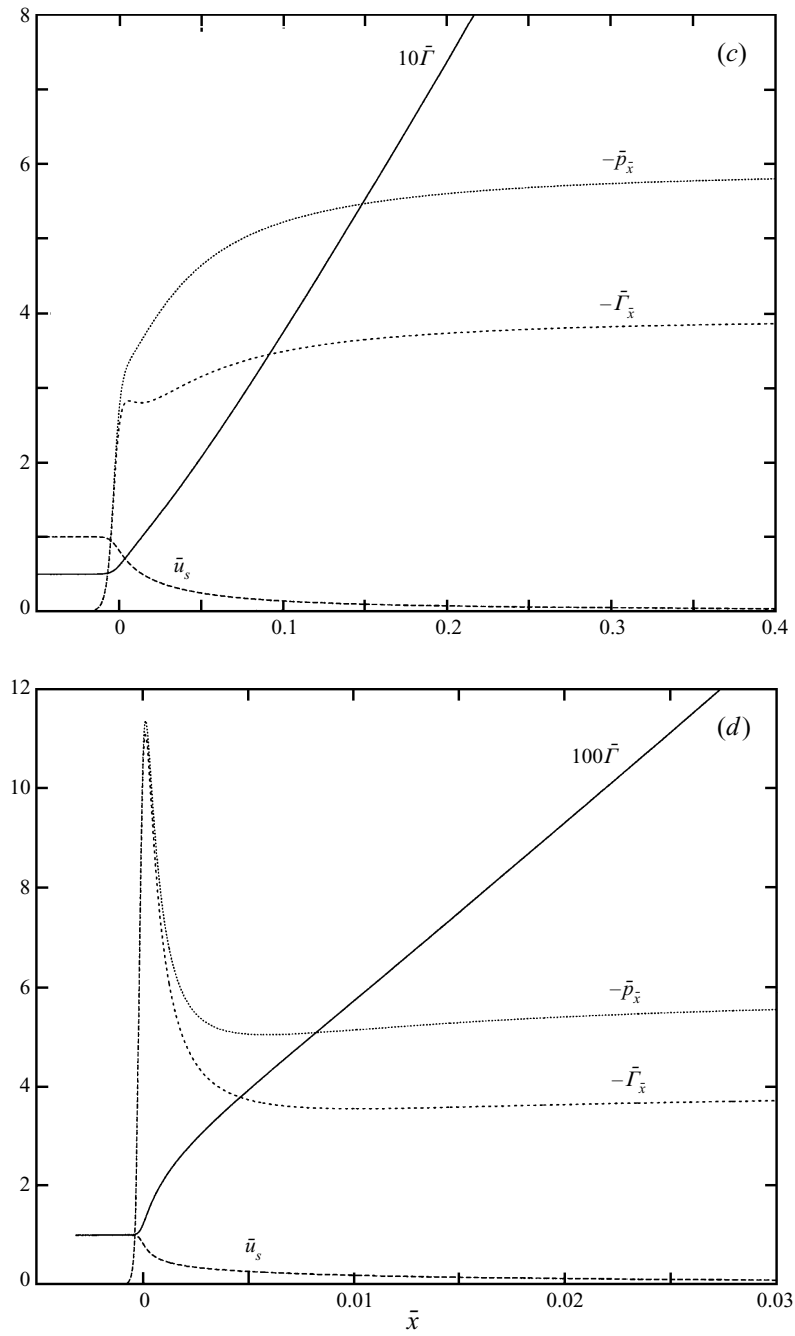FIGURE 7 Solutions using an integral approximation (5.7b) of (2.6)–(2.8) for $\mathscr{J} =$ (a) 1, (b) 0.1, (c) 0.05, (d) 0.01. Plotted in each case are $\bar{\Gamma}$ (solid; 10$\bar{\Gamma}$ and 100$\bar{\Gamma}$ are plotted in c, d respectively), $\bar{u}_s$ (dashed, $\bar{u}_s \to 1$ upstream), $-\bar{\Gamma}_{\bar{x}}$ (dotted, $-\bar{\Gamma}_{\bar{x}} \to 4$ downstream), $-\bar{p}_{\bar{x}}$ (dashed, $-\bar{p}_{\bar{x}} \to 6$ downstream). In each case the origin is chosen to be the maximum value of $-\bar{u}_{s\bar{x}}$, which is plotted dot-dashed in (a) and (b); in (c) and (d) this maximum is approximately 32.2 and 694 respectively. Note that different $\bar{x}$ ranges are used in each figure.

where $\check{W}(\alpha) \sim 4/\alpha^2$ for $\alpha \to 0$ and $\check{W}(\alpha) \sim 1/\alpha$ as $\alpha \to \infty$. The corresponding velocity profile (plotted in figure 6 for various values of α) is given by

$$u'(y) = p'\check{V}(y;\alpha), \qquad \check{V}(y;\alpha) = -1 + \cosh \alpha y + \left(\frac{\alpha - \sinh \alpha}{\cosh \alpha - 1}\right)\sinh \alpha y. \qquad (5.3a,b)$$

For $\mathscr{J} \gg 1$, (5.2), (5.3a,b) yield the return-flow lubrication-theory solution with

$$\alpha^2 \sim 4/\mathscr{J}, \quad u' \sim p'\alpha^2 \left(\tfrac{1}{2}y^2 - \tfrac{1}{3}y\right), \quad \psi' = -\tfrac{1}{4}\alpha^2 \Gamma'(y^3 - y^2), \quad \Gamma' = -\tfrac{2}{3}p' \qquad (5.4a\text{--}d)$$

where $p' < 0$. When $\mathscr{J}$ is small, α is large and the velocity profile develops boundary layers, evident in figure 6 and the approximation $\check{V} \sim -1 + \mathrm{e}^{-\alpha y} + \alpha \mathrm{e}^{-\alpha(1-y)}$. These boundary layers echo regions I and III in figure 3(a).

5.2. *An integral approximation*

Given the close resemblance between figures 2 and 6, we can use (5.3a,b) as the basis of an integral approximation of (2.6)–(2.8). We set $\bar{u}(\bar{x}, y) = 1 - A\check{V}(y;\alpha)$ for some functions $A(\bar{x})$, $\alpha(\bar{x})$. This profile satisfies $\int_0^1 \bar{u}\,\mathrm{d}y = 1$ and $\bar{u}|_{y=0} = 1$. The boundary conditions (2.8b,c) give

$$\bar{\Gamma}_{\bar{x}} = A\alpha\left(\frac{\alpha\cosh\alpha - \sinh\alpha}{\cosh\alpha - 1}\right), \quad \bar{u}_s\bar{\Gamma} = \mathscr{J}, \quad \bar{u}_s = 1 - A\left(\frac{2 - 2\cosh\alpha + \alpha\sinh\alpha}{\cosh\alpha - 1}\right)$$
$$(5.5a\text{--}c)$$

where $\bar{u}_s \equiv \bar{u}(\bar{x}, 1)$. Since the integral form of (2.6) implies that for this velocity profile the momentum flux is uniform, it is preferable to evaluate (2.6) along $y = 0$ and $y = 1$, subtract to eliminate the pressure gradient (given by $\bar{p}_{\bar{x}} = \bar{u}_{yy}|_{y=0} = -A\alpha^2$) and then

$$\bar{u}_s\bar{u}_{s\bar{x}} = \left[\bar{u}_{yy}\right]_0^1 = A\alpha^2\left[2 - \frac{\alpha\sinh\alpha}{\cosh\alpha - 1}\right] = \alpha^2(\bar{u}_s - 1). \qquad (5.6)$$

Eliminating A from (5.5a,c), it follows that $\bar{\Gamma}_{\bar{x}} = \alpha^2\check{W}(\alpha)(1 - \bar{u}_s)$ where $\check{W}$ is given by (5.2). With (5.5b) and (5.6) the system is now closed and, remarkably, the two ODE's decouple to give a first-order system, which may be expressed either as

$$\bar{u}_s\bar{u}_{s\bar{x}} = -\alpha^2(1 - \bar{u}_s), \quad \bar{u}_s^3 = \mathscr{J}/\check{W}(\alpha), \quad \bar{\Gamma} = \mathscr{J}/\bar{u}_s \qquad (5.7a)$$

or equivalently

$$\mathscr{J}^2\bar{\Gamma}_{\bar{x}} = \alpha^2\bar{\Gamma}^3\left(1 - \frac{\mathscr{J}}{\bar{\Gamma}}\right), \quad \bar{\Gamma}^3 = \mathscr{J}^2\check{W}(\alpha), \quad \bar{u}_s = \frac{\mathscr{J}}{\bar{\Gamma}}. \qquad (5.7b)$$

Far upstream ($\bar{x} \to -\infty$), with $\bar{\Gamma} = \mathscr{J} + \varepsilon\bar{\Gamma}'\mathrm{e}^{\alpha^2\bar{x}}$, we recover the linearized solution of §5.1. Far downstream (where $A\alpha^2 \sim 6$, $\alpha \to 0$ and $\bar{\Gamma} \gg 1$), $\bar{\Gamma}_{\bar{x}} \sim 4$ at leading order, as expected from lubrication theory.

A range of solutions of (5.7b) are shown in figure 7. In each case the pressure distribution has a similar shape to the surfactant distribution. For large $\mathscr{J}$ ($\alpha \to 0$), (5.7b) simplifies to $\bar{\Gamma}_{\bar{x}} \sim 4(1 - \mathscr{J}/\bar{\Gamma})$, exactly as predicted by lubrication theory for the contaminant transition region at the leading edge of a monolayer on a flat film (compare figure 7a with $\mathscr{J} = 1$ to figure 2 of Part 1; see also equation (2.12) in Part 1). The surface velocity $\bar{u}_s$ falls monotonically, and there is a weak peak of surface compression $-\bar{u}_{s\bar{x}}$. The maximum value of $-\bar{u}_{s\bar{x}}$ is 0.617 in figure 7(a) and 0.593 using the lubrication-theory approximation, a difference of less than 4%. The negative surface stress $-\bar{\Gamma}_{\bar{x}}$ and negative pressure gradient $-\bar{p}_{\bar{x}}$ rise smoothly to their downstream values 4 and 6 respectively. If the level of contaminant is reduced

(e.g. figure 7*b*, $\mathscr{J} = 0.1$), the lengthscale over which this change occurs is reduced, and the degree of surface compression increases appreciably, although $\bar{\Gamma}_{\bar{x}}$ and $\bar{p}_{\bar{x}}$ remain monotonic. Further reduction in $\mathscr{J}$, to 0.05 (figure 7*c*), greatly increases the level of surface compression, and the shear stress distribution develops a weak local maximum, although the pressure gradient remains monotonic. For $\mathscr{J} < 0.037$ the pressure gradient has a local maximum. When $\mathscr{J} = 0.01$ (figure 7*d*), both the shear stress and pressure gradients have strong local maxima over a very short lengthscale, giving rise to strongly inflectional surfactant and pressure distributions. The free-surface perturbation h_1 (see (2.2)) is therefore predicted to be inflectional for $\mathscr{J} < 0.037$, having a shape similar to the monotonic pressure distribution sketched in figure 3(*b*). Figure 7 therefore demonstrates how the stress singularity first begins to manifest itself as $\tilde{\gamma}$ is reduced.

Figure 8(*a*) demonstrates how the lengthscale of the stress distribution depends on $\mathscr{J}$; there is a striking similarity with the purely viscous solution in figure 8(*b*) of Part 1. Consistent with §4.1, as $\mathscr{J} \to 0$ the stress peak scales like $1/\mathscr{J}$, and the surface compression like $\mathscr{J}^{-2}$, over an $\bar{x}$-lengthscale $1/\mathscr{J}^2$. After a corresponding rescaling, using $\bar{\Gamma} = \mathscr{J}\check{G}(\check{x})$, $\bar{x} = \mathscr{J}^2\check{x}$, (5.7*b*) reduces to $\check{G}_{\check{x}} = (\check{G}-1)/\check{G}^4$, which has the solution $\frac{1}{4}\check{G}^4 + \frac{1}{3}\check{G}^3 + \frac{1}{2}\check{G}^2 + \check{G} + \log(\check{G}-1) = \check{x} - \check{x}_0$ where $\check{x}_0$ is a constant. Figure 8(*b*) shows the corresponding inner solution of the integral model, which is a reasonable qualitative approximation of the asymptotically correct boundary-layer solution for region V′ shown in figure 4. The pressure gradient and the stress distribution (the larger peak in figure 8*b*) are identical in this approximation. This inner solution matches downstream onto an outer region (equivalent to region I in figure 3) in which $\bar{\Gamma} \gg \mathscr{J}$ and the free surface is nearly immobile, with $\bar{\Gamma} \sim (4\mathscr{J}\bar{x})^{1/4}$. Although $\bar{\Gamma}$ should scale in this region like $\bar{x}^{1/2}$ as $\mathscr{J} \to 0$, this is only a modest deficiency and this simple integral model provides an effective means of capturing the dominant features of solutions of (2.6)–(2.8).

Finally, it is instructive to plot the the streamfunction in the frame of the wall and the vorticity distribution when inertial forces are large, to show how the return-flow streamlines are 'closed' beneath the tip of an advancing monolayer. Figure 9 shows these quantities computed using the integral approximation for the case $\mathscr{J} = 0.03$; the direction of the flow has been reversed, to allow direct comparison with figure 4 of Part 1. Although the spreading monolayer does not have a well-defined leading edge, there is a clear boundary beyond which it has no influence (although we are here neglecting the weak upstream interaction associated with a Reynolds ridge). Beneath the near-singularity in the vorticity distribution there is very strong downward displacement of fluid. Streamwise variations in vorticity decay rapidly with $\bar{x}$, indicating (as anticipated in §3) that the boundary layers along $y = 0$ and $y = 1$ grow rapidly across the fluid layer.

6. Discussion

By assuming that gravity strongly suppresses free-surface deformations ($\mathscr{G} \gg 1$), and that suitable constraints apply to the monolayer speed, length and contaminant strength ($1 \ll (\tilde{\mathscr{R}}, \tilde{\gamma}) \ll 1/\epsilon$), it has been possible to construct an asymptotically uniform description of the flow near the tip of a spreading monolayer using quasi-steady boundary-layer theory. At high Reynolds numbers the integrable tip singularity has a profound effect on the local flow, even under conditions in which it is regularized by weak contaminant. It gives rise, for example, to highly non-uniform surface shear-
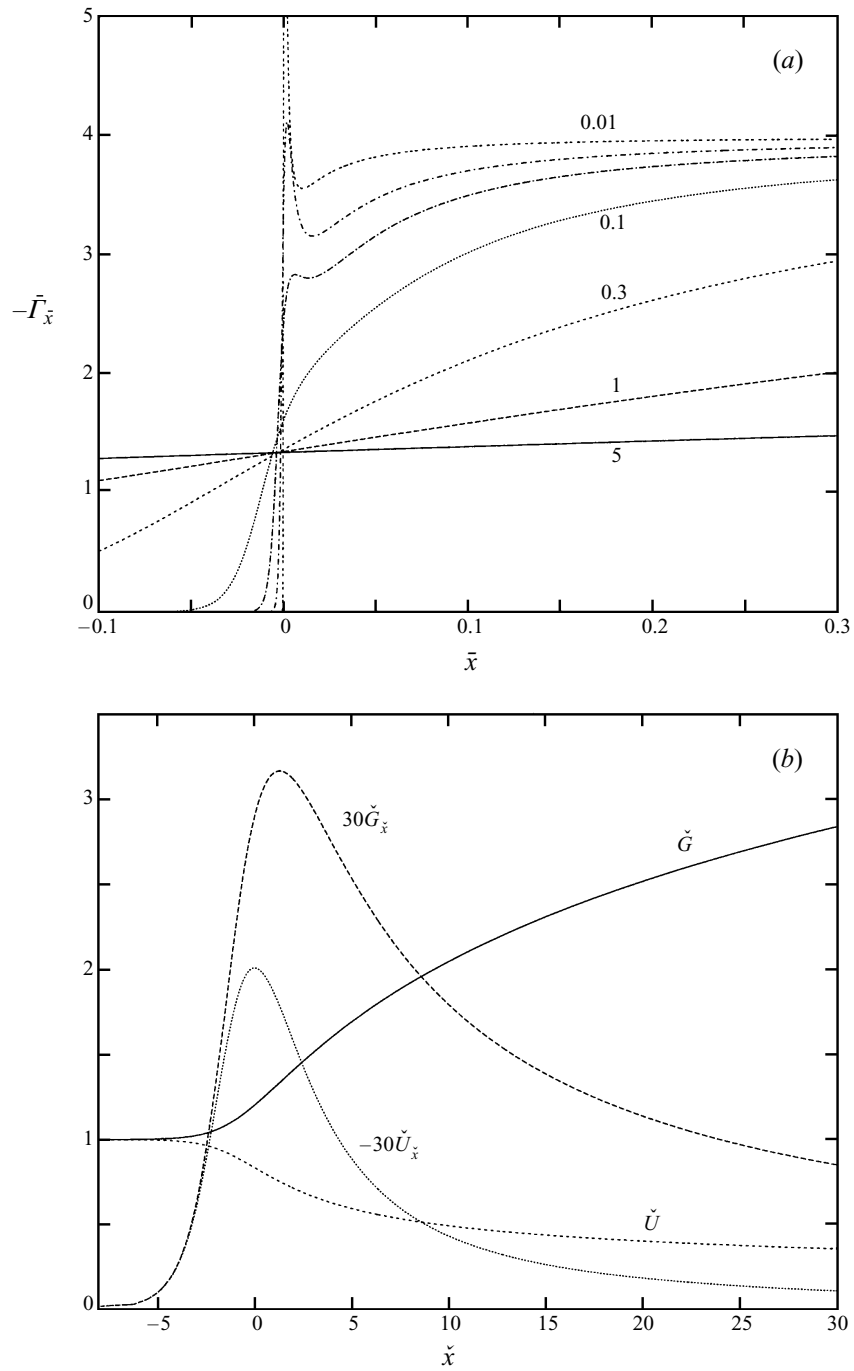
FIGURE 8. (*a*) The surface shear-stress distribution $-\bar{\Gamma}_{\bar{x}}$ computed using (5.7*b*) for $\mathscr{J} \equiv \tilde{\gamma}/\tilde{\mathscr{R}} = 0.01$ (dotted), 0.03, 0.05, 0.1, 0.3, 1, 5 (solid). (*b*) The local solution for the stress peak, plotting $\check{G} = \overline{\Gamma}/\mathscr{J}$ (solid), $30\,\check{G}_{\check{x}}$ (upper peak), $\check{U} = 1/\check{G}$ (dotted) and $-30\,\check{U}_{\check{x}}$ (lower peak).
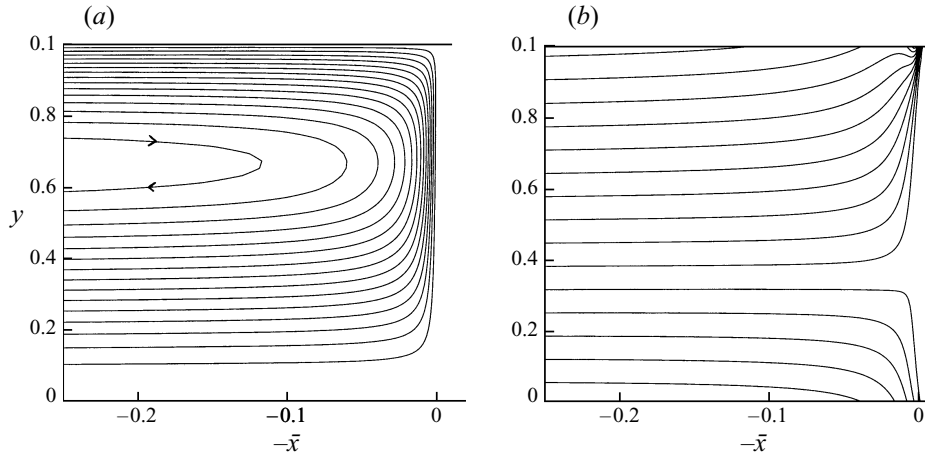
FIGURE 9. The streamfunction (*a*) and vorticity distribution (*b*) for the case $\mathscr{J} = 0.03$, plotted versus $-\bar{x}$. The monolayer is advancing from left to right with respect to $y = 0$; the vorticity increases linearly from -2 to $+4$ where there is a return flow.

stress distributions (e.g. figures 4*b*, 8*a*) which, like their purely viscous conterparts (Part 1), vary over lengthscales much shorter than the monolayer length. Perhaps the most striking manifestation of the singularity at high Reynolds numbers is the generation of the thin-film analogue of a Reynolds ridge (figures 3*b*, 5), a small hump at the free surface having length comparable to the undisturbed film thickness H^*, which arises from inertially generated pressure fluctuations associated with the abrupt change in boundary conditions at the monolayer tip. This mechanism of film deformation is quite distinct from that often described in the context of surfactant-driven flows, in which deformations originate in spatially non-uniform fluxes of the fluid layer (e.g. Gaver & Grotberg 1990; Jensen 1995).

One aim of the present study was to assess the accuracy of conventional thin-film approximations of the length of a spreading localized monolayer. Lubrication theory typically predicts that the leading-order monolayer length $L_0^* \propto t^{*\lambda}$ at time t^* for some $\lambda > 0$ (e.g. Jensen & Grotberg 1992). Thus $V^* \propto \lambda L_0^*/t^*$, so that the condition $1 \ll \tilde{\mathscr{R}} \ll 1/\epsilon$ is equivalent to $T_v^* \ll t^* \ll T_v^*/\epsilon$ where $T_v^* = \rho^* H^{*2}/\mu^*$ is the timescale for the vertical viscous diffusion of vorticity across the fluid layer. Within this time window the inertial length correction is $O(H^*\tilde{\mathscr{R}})$, or more precisely

$$L^*(t^*) \sim L_0^*(t^*) \left(1 - \tfrac{1}{4}\overline{\Upsilon}\lambda\frac{T_v^*}{t^*}\right) + O(H^*), \tag{6.1}$$

where $\overline{\Upsilon} = \Upsilon/\tilde{\mathscr{R}}$ (see (2.4)) was estimated in §3 to be less than 0.1. We can therefore assess the accuracy of the heuristic finite-depth model proposed in Jensen (1995), which neglected the presence of the boundary layer along $y = 0$ (e.g. figure 1) and assumed a relatively long development length on the $H^*\tilde{\mathscr{R}}$-scale, thereby predicting that inertial effects remain significant over times of approximately $85T_v^*$. Despite recent experimental evidence consistent with this simple model (de Ryck 1997), the more sophisticated treatment here suggests that this estimate is (at least) an order of magnitude too large, since according to (6.1) the time at which $\mathrm{d}(\log L^*)/\mathrm{d}(\log t^*)$ is within 10% of λ (the criterion used in Jensen 1995) is only $\tfrac{5}{2}\overline{\Upsilon}T_v^* < T_v^*/4$. Inertial effects therefore decay substantially quicker than previously believed. The very short development lengths make this asymptotic approach unreliable at only
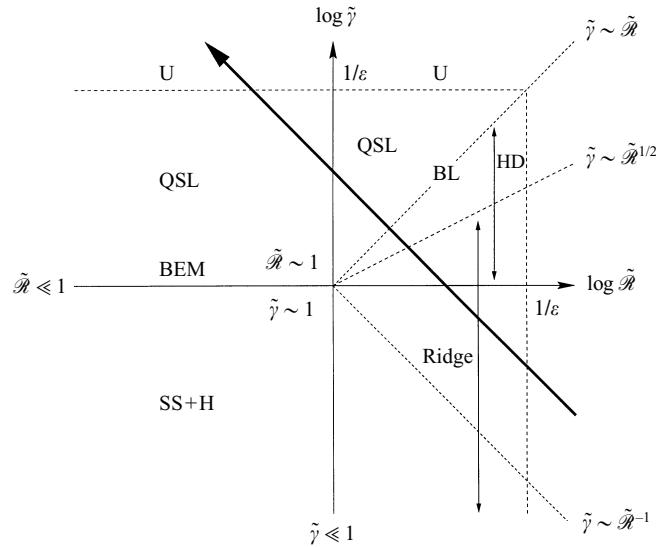
FIGURE 10. A schematic view of $(\log \tilde{\mathscr{R}}, \log \tilde{\gamma})$-space, for a long monolayer ($\epsilon \ll 1$) on a flat film. The evolution of a typical experiment along a line of constant $\tilde{\gamma}\tilde{\mathscr{R}} \gg 1$ is illustrated with a thick arrow. The abbreviations, explained in the text, denote the appropriate flow approximations in different regions of parameter space.

moderately large values of $\tilde{\mathscr{R}}$, however, so these predictions should be confirmed by full numerical treatment of the present flat-film problem, and of the other members of the family of Navier–Stokes problems at the monolayer tip (see figure 3 in Part 1) for which the film depth $h \geqslant 1$ and the horizontal flux $Q = h - 1 \geqslant 0$; such studies will yield accurate development lengths, indications of stability (inflectional velocity profiles can be anticipated if $h > 1$), and details of flows near the stress singularity. Such calculations would also provide insights into the potentially rich range of (still unexplored) interactions between inertial, gravitational and capillary forces acting at the tip of a spreading monolayer on a deforming interface.

To help put the results of this study into context, figure 10 shows schematically the different parameter regimes in the $(\log \tilde{\mathscr{R}}, \log \tilde{\gamma})$-plane considered here and in Part 1 for a monolayer spreading on a flat film. In a typical spreading experiment the speed of advance of the monolayer tip falls, but the quantity $\tilde{\gamma}\tilde{\mathscr{R}} = \rho^* H^* S_\infty^* / \mu^{*2}$ (a Suratman number) remains constant. This corresponds to moving up a line of slope -1 in the $(\log \tilde{\mathscr{R}}, \log \tilde{\gamma})$-plane, as illustrated by the thick arrow in figure 10. This example, for which $\tilde{\gamma}\tilde{\mathscr{R}} \gg 1$, is readily achievable when one considers that for a 1 mm layer of water, $\mu^{*2}/\rho^* H^* \approx 10^{-3} \mathrm{g \ s^{-2}}$, which is at least four orders of magnitude smaller than the mean interfacial surface tension of water. Ensuring that surface tension fluctuations due to contaminant are substantially smaller than $10^{-3} \mathrm{g \ s^{-2}}$ presents a significant technical challenge in any experiment.

The left-half-plane of figure 10 for which $\tilde{\mathscr{R}} \ll 1$ was treated in Part 1: with increasing $\tilde{\gamma}$, the appropriate solution methods involved the viscous stick-slip flow with Harper's (1992) asymptotics (SS+H), a boundary-element solution (BEM), the quasi-steady transition region obtainable by lubrication theory (QSL, figure 2 of Part 1) and, once $\tilde{\gamma} \sim 1/\epsilon$, the unsteady evolution (U) may be described using a nonlinear diffusion equation ((2.9a) in Part 1). Detailed calculations in Part 1 showed that the lubrication-theory approximation is accurate to within 4% for $\tilde{\gamma} \geqslant 1$ when $\tilde{\mathscr{R}} \ll 1$.

The introduction of inertia to the system complicates the picture substantially, and our treatment is correspondingly less complete (see the right-half-plane of figure 10). As long as $\tilde{\gamma} = O(1)$ or smaller, and $1 \ll \tilde{\mathscr{R}} \ll 1/\epsilon$, some part of the flow requires solution of a Navier–Stokes problem, although over long lengthscales the picture of the developing flow in §3 applies (see figures 1 and 2). For $\tilde{\gamma} \ll 1/\tilde{\mathscr{R}}$, Harper's (1992) purely viscous asymptotics may be used to regularize the stress singularity. For $1 \ll \tilde{\gamma} \ll \tilde{\mathscr{R}}$ (the region denoted HD in figure 10), the canonical boundary-layer problem treated approximately by Harper & Dixon (1974) and numerically in §4.1 (see figure 4) applies in a thin domain at the monolayer tip (region V$'$ in figure 3), smoothing the singularity at the tip of the subsurface Blasius boundary layer. As $\tilde{\gamma}$ increases further, the lengthscale over which contaminant smooths the singularity increases, so that the flow may be described first by the boundary-layer equations applying throughout the flow (when $\mathscr{J} = \tilde{\gamma}/\tilde{\mathscr{R}} = O(1)$, the region denoted BL in figure 10), and then for larger $\tilde{\gamma}$ the purely viscous quasi-steady (QSL) or unsteady (U) lubrication theory applies. The BL to QSL transition was explored using a simple integral approximation of the boundary-layer equations (2.6)–(2.8) in §5; the evolution of the surface stress distribution, for example, is shown in figure 8(a). The model predicts, for example, that once $\mathscr{J} > 0.05$ approximately (figure 7, 8a) the stress and the pressure gradient in the channel are both monotonic, so that the free surface is non-inflectional (with a shape resembling the $\overline{\Gamma}$-curve in figure 7a). Our calculations showed that lubrication theory achieves better than 4% accuracy for $\mathscr{J} \geqslant 1$ when $1 \ll \tilde{\mathscr{R}} \ll 1/\epsilon$.

An important feature of the flow for $\tilde{\gamma} = O(\tilde{\mathscr{R}}^{1/2})$ is the generation of the thin-film version of a Reynolds ridge. Above the line $\tilde{\gamma} \sim \tilde{\mathscr{R}}^{1/2}$ in figure 10 the pressure and the free-surface displacement remain monotonic functions of the streamwise coordinate x, although for $1 \ll \tilde{\gamma} < 0.05\tilde{\mathscr{R}}$ the free surface has an inflection point near the regularized singularity (much like the $\overline{\Gamma}$ distribution in figure 7d). For sufficiently rapidly spreading monolayers, however, there is an inviscid response beneath the advancing monolayer tip which yields a short-lengthscale elevation of the free surface (figure 5). The ridge exists for $\tilde{\gamma} < 3^{-1/4}\tilde{\mathscr{R}}^{1/2}$ approximately (§4.2). The shape of this structure differs from predictions (by Harper & Dixon 1974, using thin-airfoil theory) and observations (Scott 1982; Warncke, Gharib & Roesgen 1996) of the shape of a ridge on infinitely deep fluid, since in the present case capillary effects may be neglected, and the pressure distribution is strongly influenced by the presence of the plane boundary, although both types of ridge share a relatively steep slope just behind the monolayer tip.

In summary, despite the many limitations of this analysis it has been demonstrated how the presence of a stress singularity, even when regularized by surface contaminant, has a profound effect on the flow near the tip of a spreading monolayer, generating a complex flow structure over lengthscales that are too short to be described by conventional lubrication theory. As figure 10 demonstrates, the singularity's effect is felt most strongly when the monolayer is spreading fast enough for inertial effects to be significant near the monolayer tip, in which case it may generate a thin-film Reynolds ridge. Experimental verification of the predictions of this theory are keenly awaited.

REFERENCES

BADR, H., DENNIS, S. C. R., BATES, S. & SMITH, F. T. 1985 Numerical and asymptotic solutions for merging flow through a channel with an upstream splitter plate. *J. Fluid Mech.* **156**, 63–81.

BORGAS, M. S. & GROTBERG, J. B. 1988 Monolayer flow on a thin film. *J. Fluid Mech.* **193**, 151–170.

CARRIER, G. F. & LIN, C. C. 1948 On the nature of the boundary layer near the leading edge of a flat plate. *Q. Appl. Maths* **6**, 63–68.

FODA, M. & COX, R. G. 1980 The spreading of thin liquid films on a water-air interface. *J. Fluid Mech.* **101**, 33–51.

GAVER, D. P. III & GROTBERG, J. B. 1990 The dynamics of localized surfactant on a thin film. *J. Fluid Mech.* **213**, 127–148.

GROTBERG, J. B. 1994 Pulmonary flow and transport phenomena. *Ann. Rev. Fluid Mech.* **26**, 529–571.

HARPER, J. F. 1992 The leading edge of an oil slick, soap film, or bubble stagnant cap in Stokes flow. *J. Fluid Mech.* **237**, 23–32.

HARPER, J. F. & DIXON, J. N. 1974 The leading edge of a surface film on contaminated water. *Proc. Fifth Australasian Conf. Hydraulics Fluid Mech., Christchurch, NZ*, vol. 2, pp. 499–505.

JENSEN, O. E. 1995 The spreading of insoluble surfactant at the free surface of a deep fluid layer. *J. Fluid Mech.* **293**, 349–378.

JENSEN, O. E. & GROTBERG, J. B. 1992 Insoluble surfactant spreading on a thin viscous film: shock evolution and film rupture. *J. Fluid Mech.* **240**, 259–288.

JENSEN, O. E. & HALPERN, D. 1998 The stress singularity in surfactant-driven thin-film flows. Part 1. Viscous effects. *J. Fluid Mech.* **372**, 273–300.

RYCK, A. DE 1997 Fragmentation of a spreading drop. *Europhys. Lett.* **40**, 305–310.

SCHLICHTING, H. 1968 *Boundary-Layer Theory*. McGraw-Hill.

SCOTT, J. C. 1982 Flow beneath a stagnant film on water: the Reynolds ridge. *J. Fluid Mech.* **116**, 283–296.

SMITH, F. T. 1977 Steady motion through a branching tube. *Proc. R. Soc. Lond.* A **355**, 167–187.

SNEDDON, I. N. 1974 *The Use of Integral Transforms*. p. 94. McGraw Hill.

STOCKER, J. R. & DUCK, P. W. 1995 Stationary perturbations of Couette–Poiseuille flow: the flow development in long cavities and channels. *J. Fluid Mech.* **292**, 153–182.

TAYLER, A. B. 1973 Singularities at flow separation points. *Q. J. Mech. Appl. Maths* **26**, 153–172.

TUCK, E. O. & BENTWICH, M. 1983 Sliding sheets: lubrication with comparable viscous and inertia forces. *J. Fluid Mech.* **135**, 51–69.

VAN DYKE, M. 1971 Entry flow in a channel. *J. Fluid Mech.* **44**, 813–823.

VOOREN, A. I. VAN DE & DIJKSTRA, D. 1970 The Navier–Stokes solution for laminar flow past a semi-infinite plate. *J. Engng Maths* **4**, 9–27.

WARNCKE, A., GHARIB, M. & ROESGEN, T. 1996 Flow measurements near a Reynolds ridge. *Trans. ASME J. Fluids Engng* **118**, 621–624.

WILSON, S.K. & DUFFY, B.R. 1998 On lubrication with comparable viscous and inertia forces. *Q. J. Mech. Appl. Maths* **51**, 105–124.